# Horizontal-Axis Wind Turbine Wake Sensitivity to Different Blade Load Distributions

Christopher L. Kelley*, David C. Maniaci†, and Brian R. Resor‡
*Sandia National Laboratories§, Albuquerque, NM, 87185, USA*

**Two different wind turbine blade designs are proposed and modeled using a free-wake, vortex lattice method, the Code for Axial and Crossflow TUrbine Simulation, CACTUS. The two designs have the same thrust coefficient as predicted by blade element momentum theory but different distributed loads across the span of the blade. In this way, the sensitivity of the wake structure due to spatial loading differences was investigated, all while keeping the integrated total drag force constant between the two designs. The first blade, design A, maximized power coefficient at a tip speed ratio of 9. The second blade, design B, increased induction over the inner 75% of the blade span, and unloaded the outer 25%. The wake of design B showed faster recovery of freestream momentum, over 10 rotor diameters sooner than design A in uniform inflow.**

## Nomenclature

| | |
|---|---|
| $a$ | axial induction factor, $1 - \frac{U}{U_\infty}$ |
| $B$ | number of blades |
| $c$ | blade section chord, m |
| $C_d$ | drag coefficient |
| $C_l$ | lift coefficient |
| $C_P$ | power coefficient |
| $C_T$ | thrust coefficient |
| $D$ | blade element drag, N |
| $F$ | tip loss factor |
| $k$ | lift-to-drag ratio, $L/D$ |
| $K$ | turbulent kinetic energy, $K = \frac{1}{2}\left(\overline{(U')^2} + \overline{(V')^2} + \overline{(W')^2}\right)$ |
| $l$ | smallest turbulent length scale resolvable, m |
| $L$ | blade element lift, N |
| $nti$ | number of time steps per revolution in vortex solution |
| $r$ | radial distance from axis of rotation, m |
| $R$ | radius of rotor swept area, m |
| $U$ | axial component of fluid velocity, m/s |
| $U_\infty$ | freestream velocity, m/s |
| $V$ | ground normal component of fluid velocity, m/s |
| $W$ | transverse component of fluid velocity, m/s |
| $x$ | axial coordinate, m |
| $y$ | ground normal coordinate, m |
| $z$ | transverse coordinate, m |
| $\alpha$ | blade section angle of attack, degrees |
| $\beta$ | blade section twist, degrees |
| $\Gamma$ | bound circulation along blade span, $m^2/s$ |
| $\Gamma'$ | dimensionless bound circulation along blade span, $\frac{\Gamma}{4\pi U_\infty R}$ |

*Postdoctoral Appointee, Wind Energy Technologies, PO Box 5800, MS 1124, Member AIAA.
†Senior Member of the Technical Staff, Wind Energy Technologies, PO Box 5800, MS 1124, Member AIAA.
‡Senior Member of the Technical Staff, Wind Energy Technologies, PO Box 5800, MS 1124, Member AIAA.
§Sandia National Laboratories is a multi-program laboratory managed and operated by Sandia Corporation, a wholly owned subsidiary of Lockheed Martin Corporation, for the U.S. Department of Energy's National Nuclear Security Administration under contract DE-AC04-94AL85000, (SAND2014–4643 A).

$\Delta t$ time step of vortex simulation, $s$, $\Delta t = \frac{2\pi}{\Omega\, nti}$
$\lambda$ tip speed ratio, $\frac{\Omega R}{U_\infty}$
$\phi$ inflow angle at blade section relative to plane of rotation$\alpha + \beta$, degrees
$\Omega$ angular velocity of rotor, rad/s

$SWiFT$ Scaled Wind Farm Technology
$\overline{x}$ time average of quantity $x$
$x'$ fluctuating part of Reynolds decomposition of quantity $x$

# I. Introduction

A major goal of the Department of Energy's National Rotor Testbed project is to study wind turbine wakes both through modeling efforts, and experiments on 225 kW wind turbines at Sandia National Laboratories' SWiFT testing facility. Vortex methods provide an opportunity to study the wake at a small computational cost compared to higher order cartesian CFD methods. Various existing vortex codes are first discussed in the Introduction. In Section II, two basic wind turbine blade geometries are designed to have different distributions of lift along the blade span but identical total thrust coefficients on the rotor plane. Section III contains the vortex simulation results. Differences in the time averaged and fluctuating velocity components are presented, which help explain the differences in momentum recovery for the two designs.

### Motivation

We are proposing that a wind turbine blade designed with a unique loading will have a unique wake. This is in contrast to existing wind turbine far-wake models where the wake only depends on the integrated thrust coefficient.

It is understood that differences in the wake due to blade load distributions appear in the near wake, approximately less than 5 rotor diameters downstream. Whereas, the far wake tends to have a self-similar shape that spreads at a nearly linear rate downstream. Far-wake models, such as those of Jensen[1] and Frandsen,[2] depend on the thrust coefficient and turbulence intensity of the atmospheric boundary layer which means that the predicted wake farther than 5 rotor diameters does not depend on the blade load distribution, only the total axial force of the wind turbine. The results in Section III show that ignoring blade load distributions ignores the differences in stability of wakes created by unique force distributions. The specific vortex method code discussed shows both the breakdown of the root and tip vortices to occur at different distances downstream and thus affect the momentum recovery, not captured by far-wake models that only depend on integrated forces.

### Vortex Methods

Vortex methods are mid-fidelity models which not only predict wind turbine performance, but also the structure of the wake. This is a distinct advantage over lower order models which only calculate fluid motion and forces local to a wind turbine blade. In addition, the computation time is significantly reduced compared to higher-order computational fluid dynamics simulations.

Various vortex methods have been developed which allow the wake to freely convect due to interaction of all the shed vortex elements summarized in Vermeer[3] et al. and Sørensen and Shen.[4] Vortex elements may be constant circulation line elements or filaments such those by Simoes and Graham,[5] Miller,[6] Bareiss et al,[7] and Afjeh and Keith.[8] Vortex elements may also be smooth distributions between discrete elements such as WIND_DVE discussed by Maniaci[9] and other work by Voutsinas.[10]

Specifically at Sandia National Laboratories, VDART is the predecessor to CACTUS and predicts the performance and wake of a Darrieus-type vertical axis wind turbine.[11] The VDART code shows the predicted power production and velocity deficits in the wake matching an experiment performed on the same geometry in a water tow-tank.[11,12]

CACTUS (Code for Axial and Crossflow TUrbine Simulation) is a Sandia National Labs developed free-wake vortex filament method for analysis of horizontal and vertical axis turbines.[13] Unsteady aerodynamics are captured using both the Leishmann-Beddoes dynamic stall model[14] and the Boeing-Vertol model of Gormont.[15] It has been validated with the Sandia 5 m and 34 m VAWT experiments and VAWT 850

which included ellipsoidal struts. More recently the CACTUS tool has been validated with a three-bladed horizontal axis hydrofoil with an experiment at Penn State's ARL and also a two-bladed turbine at the US Naval Academy.[16] The power coefficient as a function of tip speed ratio predicted by CACTUS matched the experiments well, especially considering hydrodynamic data came from XFOIL and not experiment. Recommended improvements to CACTUS include rotational stall delay effects. Design through optimization integrated with Sandia's DAKOTA project has already begun being implemented by the Water Energy Technologies Department at Sandia National Laboratories.

The method of solution for these free wake vortex models steps forward in time until the power over one rotor revolution has converged. Vortex filaments are shed along blade trailing edge to freely interact and convect downstream in the wake. The solution method is summarized as follows:

- The strength of each shed *streamwise* vortex filament is determined by the local slope of bound circulation calculated from the Kelvin Circulation Theorem, similarly to Prandtl Lifting Line Theory.
- The strength of the *spanwise* shed vorticity is equal to the time rate of change of bound circulation. These two types of shed vortex filaments keep the material derivative of circulation equal to zero, $\frac{D\Gamma}{Dt} = 0$.
- The Biot-Savart Law is used to calculate the induced velocity on every vortex filament in the wake due to every other filament and the bound circulation. It is also used to calculate the induced velocity and hence local flow angle along the blade quarter-chord.
- Blade forces are calculated using the user-supplied aerodynamic data for the various airfoil sections of the design. These forces are integrated to calculate power.
- Vortex filaments are convected and the blade is rotated one time-step.
- This process is repeated until the power has sufficiently converged to a final solution for a steady inflow, zero yaw error simulation, or the phase averaged power has converged for an unsteady solution. Details of the governing equations are summarized in the original summary of VDART by Strickland et al.[11]

## II. Blade Designs

For the proposed designs of this work, axial induction factors, and hence circulation across the blade were specified. However, vortex methods do not allow one to know the proper chord and twist distribution for a specified load distribution unless by iteration. To speed up the process, the chord and twist of the blade designs were determined according to blade element momentum theory (BEMT).

### Design A – $C_{P_{max}}$

This proposed blade was designed to have a maximum power coefficient for a tip speed ratio, $\lambda = 9$. The airfoil distribution along the span was chosen to be similar to other blade designs which start with thick airfoils near the blade root and thin airfoils near the blade tip. The operating angle of attack and lift coefficient were chosen for each airfoil's maximum lift-to-drag ratio. A summary of the chosen airfoil locations, their maximum lift-to-drag ratios, and the corresponding lift coefficients and angle of attacks for design A are seen in Table 1. Rough airfoil data were used for the NACA $63_6$-618 airfoil to be better representative of a soiled/eroded blade in operation.

Different 3D effects are included into BEMT such as the effect of wake rotation, drag, and losses modeled using the Prandtl model. The formulation of these effects and the conservation equations are shown in Burton et al.[17] To achieve a maximum power coefficient at a tip-speed-ratio of 9, the axial induction factors (azimuthal averages) to maximize $C_P$ are shown in Figure 1. The axial induction factor used on the first 25% of the blade span was from including the effects of drag and wake rotation. For the outer 75% of the blade span, the axial induction factor was from Prandtl's tip loss model. This induction factor distribution is called '2575' and is seen in Figure 1.

The chord and twist of the blade which produces the target axial induction factor can be found according to the following relationships seen in Jamieson,[18] and summarized in the following equations. Let $\frac{r}{R}$ be

**Table 1. AIRFOILS AND OPERATING POINTS FOR DESIGN A**

| Section | Shape | $\frac{r}{R}$ | $\frac{L}{D}_{max}$ | $C_l$ | $\alpha^\circ$ |
|---|---|---|---|---|---|
| 1 | Circle | $0 \leq \frac{r}{R} < 0.125$ | 0 | 0 | 0 |
| 2 | DU 40 | $0.125 \leq \frac{r}{R} < 0.225$ | 59.6 | 0.86 | 5 |
| 3 | DU 35 | $0.225 \leq \frac{r}{R} < 0.375$ | 90.2 | 1.26 | 8 |
| 4 | DU 30 | $0.375 \leq \frac{r}{R} < 0.475$ | 96.5 | 1.25 | 8 |
| 5 | DU 25 | $0.475 \leq \frac{r}{R} < 0.675$ | 134.6 | 1.06 | 5 |
| 6 | NACA $63_6$-621 | $0.675 \leq \frac{r}{R} < 0.825$ | 144.9 | 1.07 | 5 |
| 7 | NACA $63_6$-618 | $0.825 \leq \frac{r}{R} \leq 1.0$ | 62.8 | 0.86 | 4 |

spanwise location, $F$ is tip loss factor, $k = L/D$, and $B = 3$ are the number of blades. First the tangential induction factor was calculated based on the target $a$, $C_l$, and $L/D$ from Table 1 according to

$$a'(\lambda, \frac{r}{R}) = \frac{[\lambda^2 k^2 (\frac{r}{R})^2 + 2\lambda k \frac{r}{R} - 4ak[\lambda \frac{r}{R} - k(1-a)] + 1]^{0.5} - (\lambda k \frac{r}{R} + 1)}{2\lambda k \frac{r}{R}}. \tag{1}$$

The blade geometry parameter, $\Lambda(\lambda, \frac{r}{R})$, is useful for calculating the chord and was found according to

$$\Lambda(\lambda, \frac{r}{R}) = \frac{8\pi a(1-a)}{B\lambda(1+a')\sqrt{(1-a)^2 + \lambda^2(\frac{r}{R})^2(1+a')^2}} \frac{F}{[1 + \frac{(1-a)}{k\lambda \frac{r}{R}(1+a')}]}. \tag{2}$$

The normalized chord is the geometry parameter divided by the lift coefficient

$$\frac{c}{R} = \frac{\Lambda(\lambda, \frac{r}{R})}{C_l(\frac{r}{R})}. \tag{3}$$

The required blade twist, $\beta$, to ensure each blade element is operating at the target angles of attack, $\alpha$, was found.

$$\beta = \arcsin\left(\frac{1-a}{\sqrt{(1-a)^2 + \lambda^2(\frac{r}{R})^2(1+a')^2}}\right) - \alpha \tag{4}$$

Due to the abrupt changes in airfoil sections along the blade span, these equations lead to steps in chord and twist, seen as red lines in Figures 2 and 3. This does not lead to a manufacturable blade. The chord and twist was then smoothed with interpolating splines between airfoil transitions along the blade span. The transition near the hub from the ideal large chord to a cylinder at the nacelle interface was made to match common blade designs inboard of the 25% normalized span location. These are the green lines of Figures 2 and 3.

### Design B – Unloaded Tip

The second rotor was designed to have the same thrust coefficient predicted from theory as design A however with an unloaded tip. Therefore the ideal axial induction factor of design A was lowered with a spline starting at the 75% span location. To keep the thrust coefficient the same, the entire new and tip unloaded $a(\frac{r}{R})$ distribution was multiplied by a constant ($C$) slightly larger than 1, such that integrating $8(r/R)C \cdot a(1 - C \cdot a) = C_T$ of design A. The constant $C = 1.2572$ lead to equal theoretical thrust coefficients $C_T = 0.857$. Figure 4 shows the integrand in finding the thrust coefficient, and it can be seen the difference in area between the two designs is zero.

Therefore, design B has a highly loaded blade ($a > 1/3$) over the first 75% of the span, and an unloaded tip ($a < a_{\text{Prandtl tip loss}}$) over the outer 25% of the blade. The nondimensional circulation distribution is proportional to the actual lift force across the blade span and can be calculated.

$$\Gamma' = \frac{\Gamma}{4\pi U_\infty R} = \frac{1}{\lambda} a(1-a). \tag{5}$$

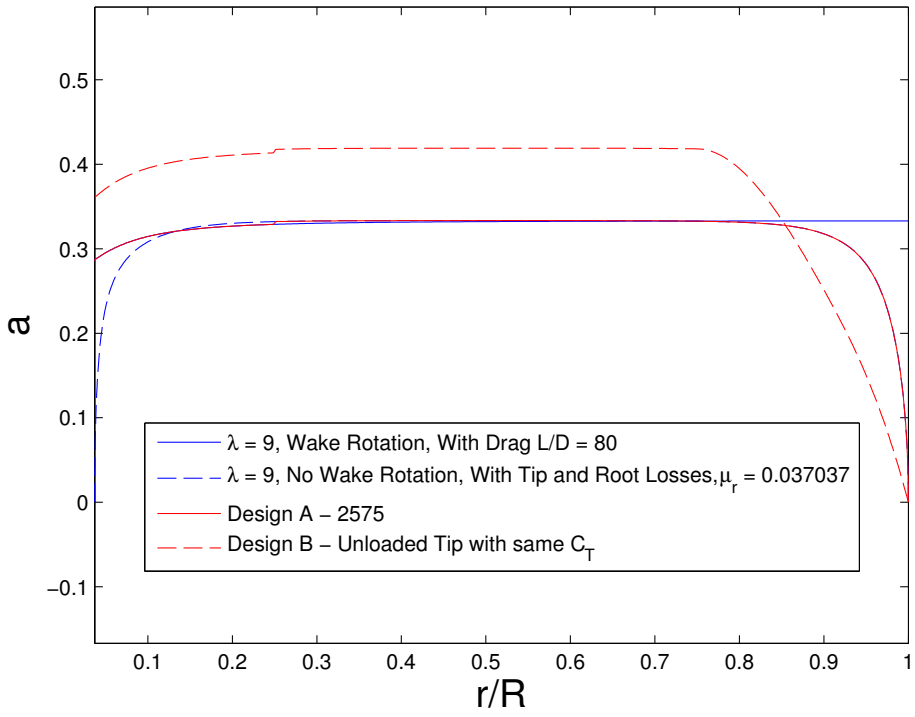


**Figure 1. Theoretical design A and B axial induction (azimuthal average) along blade span.**

As seen in Figure 5, design B has higher loading across the first 75% of the span, and is unloaded near the tip. This produces a suboptimal power coefficient for design B. Two blade designs with the same thrust coefficient and different load distributions help answer the question of wake sensitivity. In addition, the axial induction factors can be checked against their intended targets comparing vortex methods to BEMT.

The final characteristics of Designs A and B are shown in Table 2.

**Table 2. DESIGN SUMMARY**

| Design | R (m) | Power $_{\Omega R=75}$ (kW) | $C_P$ | $C_T$ | $U_\infty$ (m/s) | $\lambda_{\text{design}}$ | $\Omega R$ (m/s) | $\Omega$ (rad/s) |
|---|---|---|---|---|---|---|---|---|
| A | 13.50 | 97.82 | 0.482 | 0.857 | 8.33 | 9 | 75 | 5.56 |
| B | 13.50 | 90.94 | 0.448 | 0.857 | 8.33 | 9 | 75 | 5.56 |

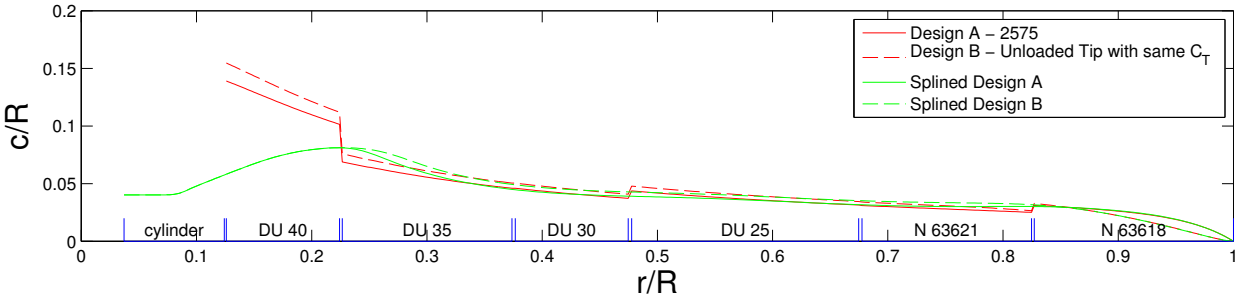


**Figure 2. Chord distribution for Designs A and B before and after spline fits.**

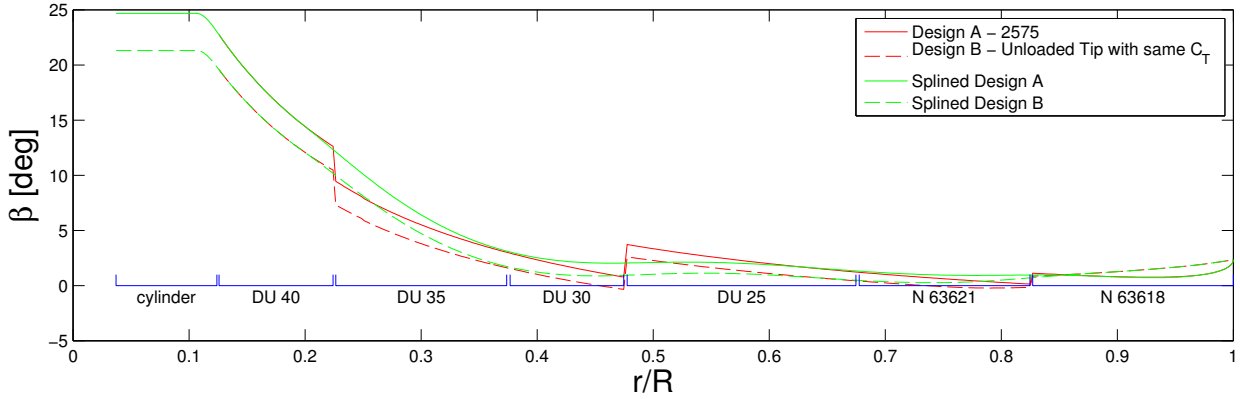


**Figure 3. Blade twist for Designs A and B before and after spline fits.**

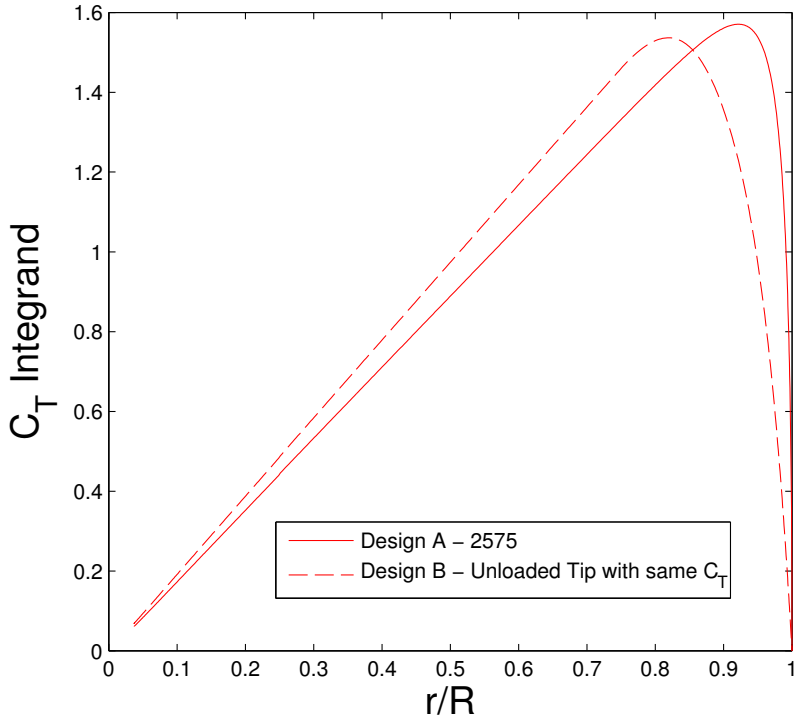


**Figure 4. Integrand of thrust coefficient showing equal area.**

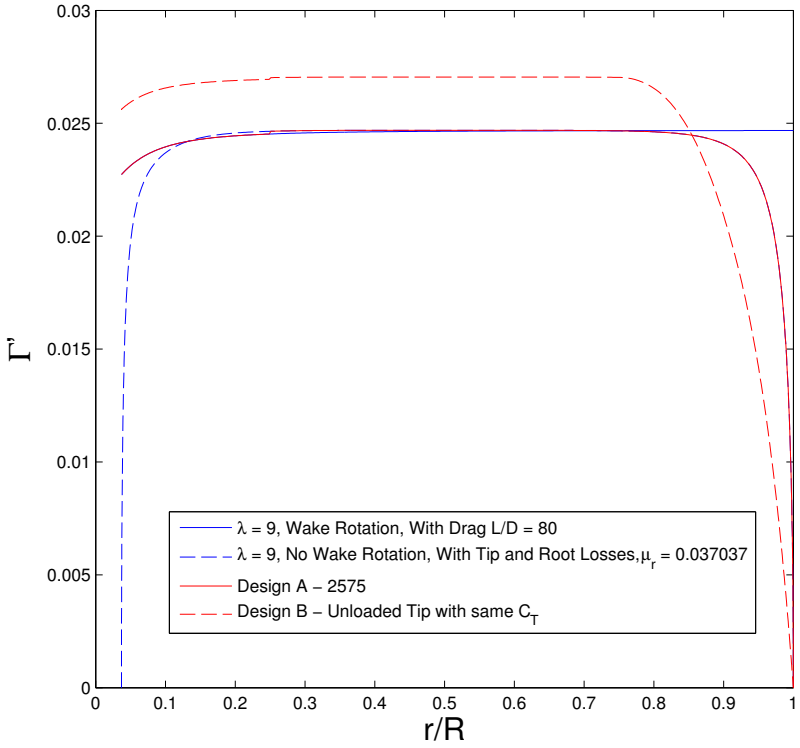


**Figure 5. Nondimensional circulation distribution.**

# III. Results

### Verification of Design

The proposed designs were input into both a blade element momentum theory code, WT_Perf, and vortex free-wake codes, CACTUS and Wind_DVE. Since the governing equations used to design the blade are nearly identical to those included in WT_Perf, the simulation matched the target axial induction factors shown in Figure 6. The only discrepancies were due the spline fit through regions where airfoils changed section shape, leading to a chord and twist that matches the target design only at the tip and near the center of each airfoil region. It should be noted that the target values in Figure 6 are relative to the blade, $\frac{a}{F}$, whereas the targets in Figure 1 were azimuthal averages.

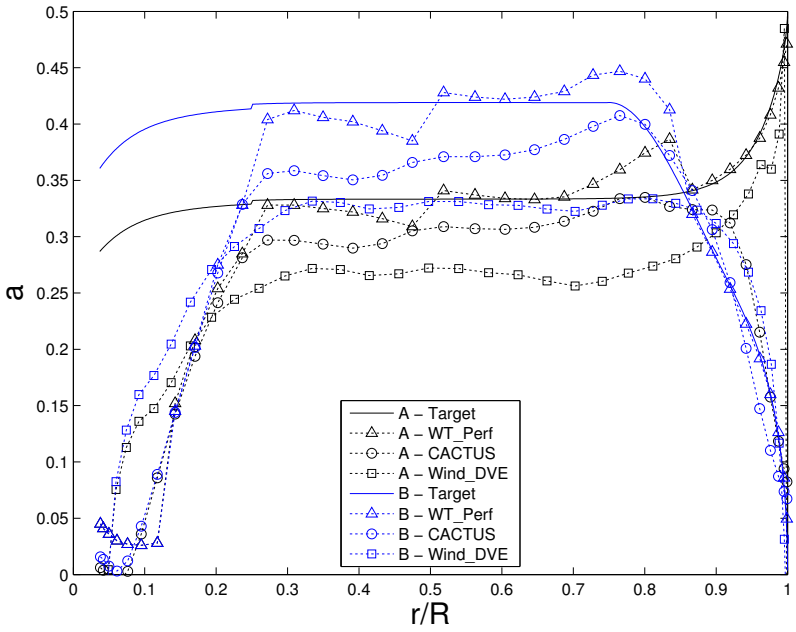


**Figure 6. Target and model predicted axial induction factors, relative to blade.**

The vortex methods predicted a lower axial induction factor across the majority of the blade span. As the number of wake elements grows, the axial induction factor rises and convergences to a solution for an infinitely long wake. However, a total of 120 revolutions were used in the vortex solutions for rotor performance so this did not explain the lower axial induction factors. This discrepancy between low and mid-fidelity modeling is common. The solution that agrees more with experiment remains an open question.

The integrated loads across the blade span predicted power and thrust coefficients. These were tabulated in Table 3. Design B has a lower efficiency as expected. CACTUS predicts an average power coefficient 5% higher and an average thrust coefficient 3% lower than blade element momentum theory. The thrust coefficient for design B as predicted by CACTUS is 2% higher than A, even though the thrust coefficients were intended to be identical.

**Table 3. BLADE PERFORMANCE at $\lambda = 9$**

| Design | $C_P$ | | $C_T$ | |
|---|---|---|---|---|
| | Target | CACTUS | Target | CACTUS |
| A | 0.482 | 0.505 | 0.857 | 0.817 |
| B | 0.448 | 0.472 | 0.857 | 0.835 |

**Wakes**

The wake was simulated in CACTUS for 120 revolutions, or approximately 80 rotor radii of freestream convection. There were 20 time steps per revolution which is a time step of $\Delta t = 0.07s$. Time-averaged and fluctuating quantities were found from revolution 80 through 120 such that the starting vortex structure did not influence the far-wake. Figure 7 shows the streamwise velocity deficits for Designs A and B as the profile evolves downstream of the rotor plane, at $\frac{z}{R} = 0$. The axial velocity deficit is higher for design B at the rotor plane as designed. Between 5 and 6 rotor radii downstream, the central jet begins to breakdown and the velocity on the axis centerline falls below $U_\infty$ for design A, which does not occur until after 6 rotor radii for design B. At 10 rotor radii downstream, both designs show self-similar Gaussian shaped profiles, with design B clearly recovering momentum faster than design A. Based on this plot the near wake for design A would be $0 < \frac{x}{R} < 6$, and $0 < \frac{x}{R} < 8$ for design B as defined by velocity deficits similar to the rotor plane. The mid-wake region would then be $6 < \frac{x}{R} < 10$ for design A and $8 < \frac{x}{R} < 10$ for design B. And finally both blade designs show Gaussian velocity profiles in the far-wake beyond $\frac{x}{R} > 10$. The contour plot of the time-averaged axial velocity field, $\frac{\overline{U}}{U_\infty}$, in Figure 8 shows the same results. The central jet between the 3 blades of the rotor collapses sooner and more abruptly for design A.

Figure 9 shows the wake width for the two blade designs. As plotted, the wake edge is defined as the upper and lower $\frac{y}{R}$ locations closest to zero where the time averaged axial velocity has exceeded 90% of the freestream velocity. Again there is clear evidence that the wake of design B is shrinking and recovering momentum faster.

The drag coefficient, which is a measure of the wake momentum deficit relative to the freestream, is presented in Figure 10. The greatest deficit is at $\frac{x}{R} = 6.2$ for design A and $\frac{x}{R} = 7.4$ for design B. For both designs this happens when the centerline axial velocity first falls below $\frac{U_\infty}{2}$. Most notable is the momentum recovery in the mid and far-wake for design B relative to A. The momentum deficit is down to 10% of the freestream (90% recovery) by $\frac{x}{R} = 34.8$ for A and $\frac{x}{R} = 24.5$ for B, a difference of over $10R$. This could mean significant reconsideration of wind turbine blade design for enhanced wake recovery. This analysis does not include turbulence and turbulent dissipation. Concurrent research using LES with a line actuator model (VWiS code at the University of Minnesota[19]) for the identical blade designs is underway.[20]

In consideration of why design B has a less stable wake that recovers momentum faster, other fluid quantities were calculated, such as vertical and azimuthal velocity, out of plane vorticity, and turbulent kinetic energy. One might think that vertical momentum transfer should clearly explain the faster momentum recovery. Figure 11 shows the time averaged vertical velocity contours, $\frac{\overline{V}}{U_\infty}$. Red are positive and up, whereas blue are negative and down. There is no clear stronger momentum flux toward the centerline in design B as one might expect. Therefore it must be the angular momentum already contained in the wake that is primarily responsible for the momentum recovery of the wake since no significant vertical velocity fluxes are evident.

Moving onto the time averaged azimuthal velocity, $\frac{\overline{W}}{U_\infty}$, Figure 12 shows that design B has greater angular momentum in its wake because the contours are darker directly behind the rotor plane. There is also an interesting swirl reversal for design A most intense at $\frac{x}{R} = 6.1$ and corresponds to the root vorticity changing signs as seen in Figure 13. This reversal is most likely due to vortex pairing but will need to be investigated in more detail. This swirl and vorticity both changing directions in the root region near the centerline also occurs, but is less intense, for design B, happening at $\frac{x}{R} = 8.4$. It remains an open question as to how this more intense vortex and swirl reversal for design A produces a more stable wake that takes longer to recover momentum.

Finally the turbulent kinetic energy is plotted in Figure 14, which confirms that the unsteady motions in the root vortex are more intense for design A despite the fact that there was a larger spanwise velocity gradient at the rotor plane for design B. In addition the highest kinetic energy is originating from the centerline, not the freestream. However, future work will look further at the effect of resolvable turbulent length scales with CACTUS. It is entirely possible that higher turbulent kinetic energy has been filtered out by the time step size, and that turbulent kinetic energy near the blade tips is larger if those time and length scales are resolved. Nonetheless, the turbulent kinetic energy distributes itself out further from the centerline for rapidly for design B, indicating that the increased tangential induction of design B promotes momentum recovery.

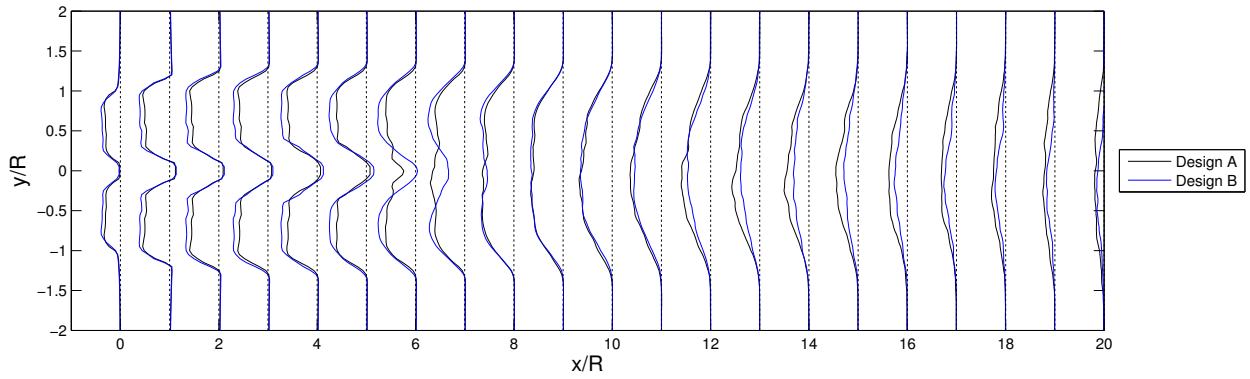


**Figure 7. Time averaged axial velocity profiles, $\frac{\overline{U}}{U_\infty}$, in wake.**

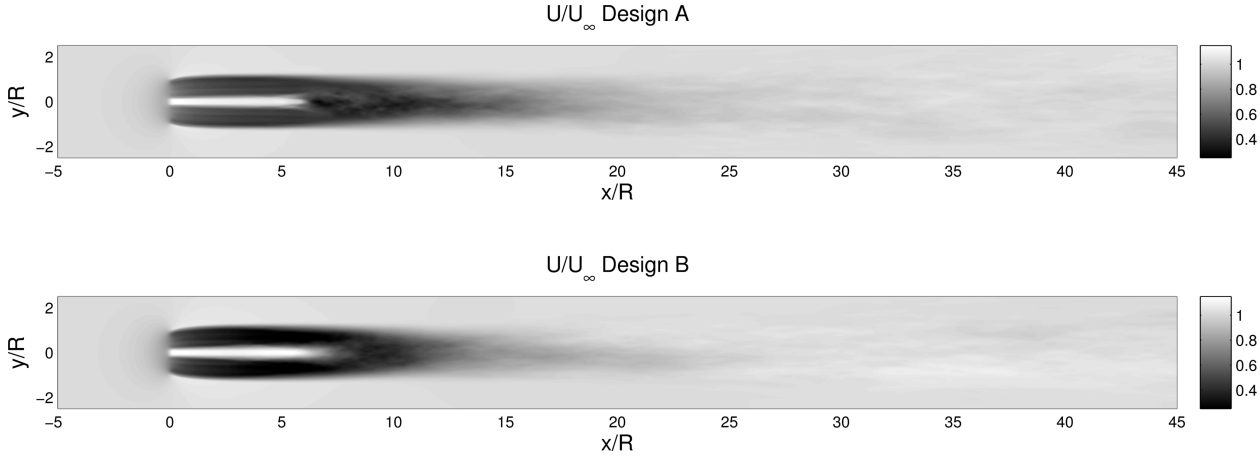


**Figure 8. Time averaged axial velocity contours, $\frac{\overline{U}}{U_\infty}$.**

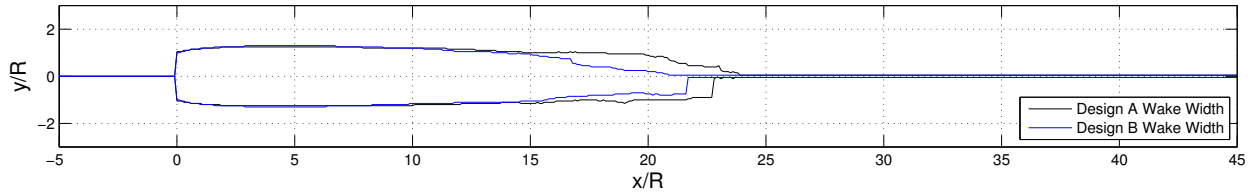


**Figure 9. Wake edge, $\frac{y}{R}\left(\frac{\overline{U}}{U_\infty} = 0.90\right)$.**

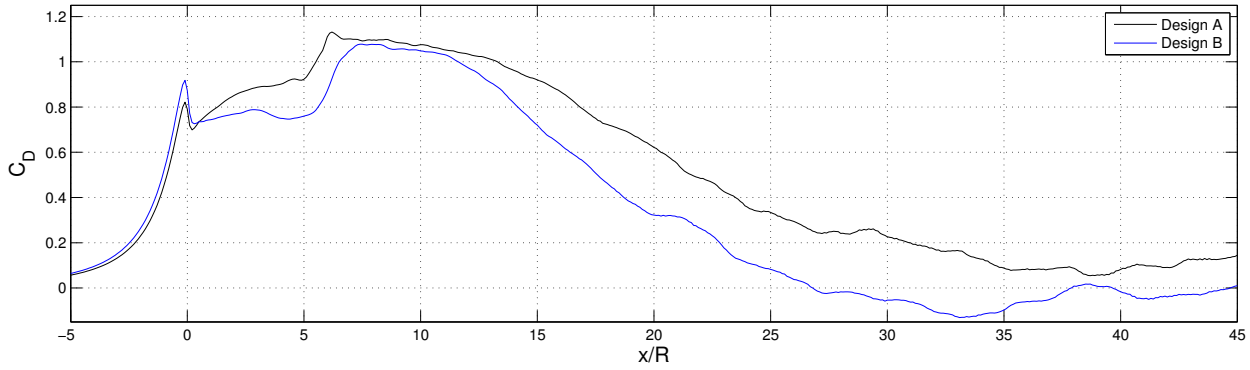


**Figure 10. Vertical plane axial momentum deficit for designs A and B.**

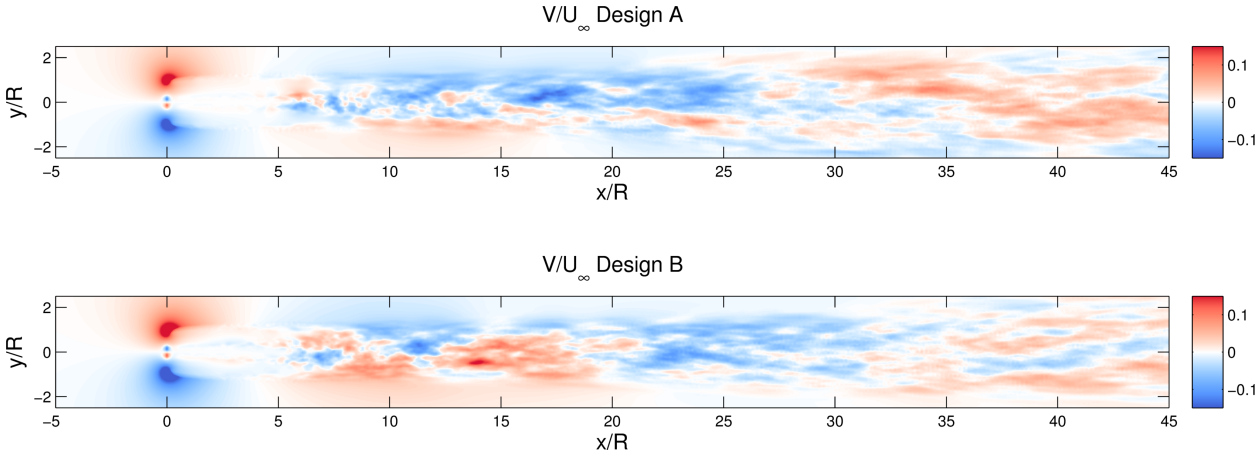


**Figure 11. Time averaged vertical velocity contours, $\frac{\overline{V}}{U_\infty}$.**

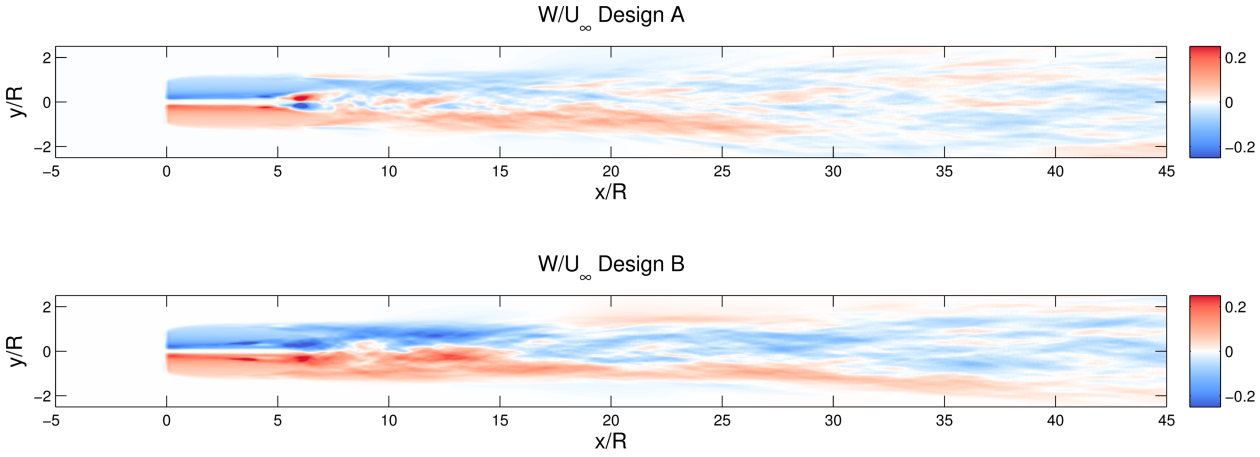


**Figure 12. Time averaged azimuthal velocity contours, $\frac{\overline{W}}{U_\infty}$.**

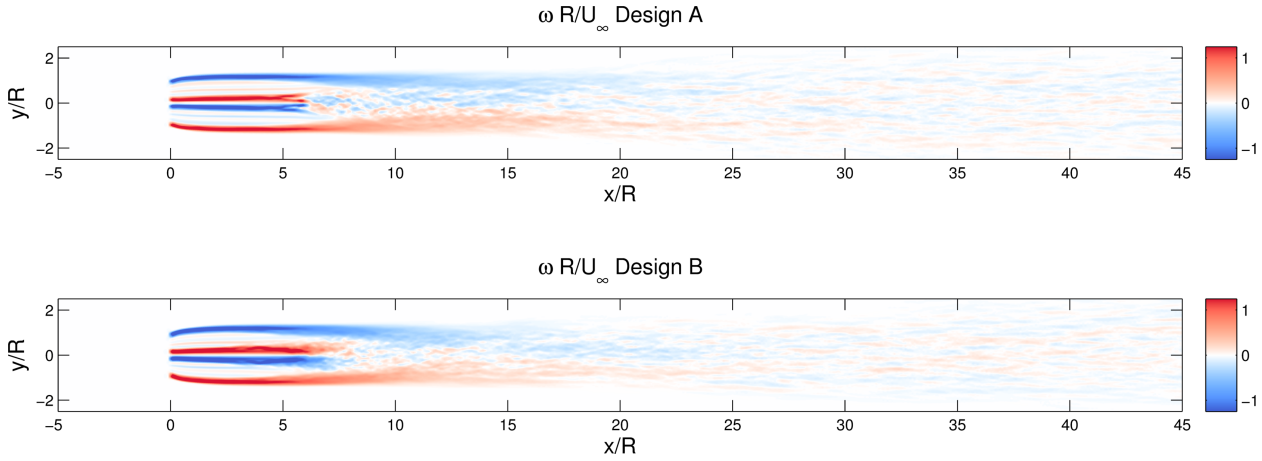


**Figure 13. Time averaged vorticity contours, $\frac{\overline{\omega}_z R}{U_\infty}$.**

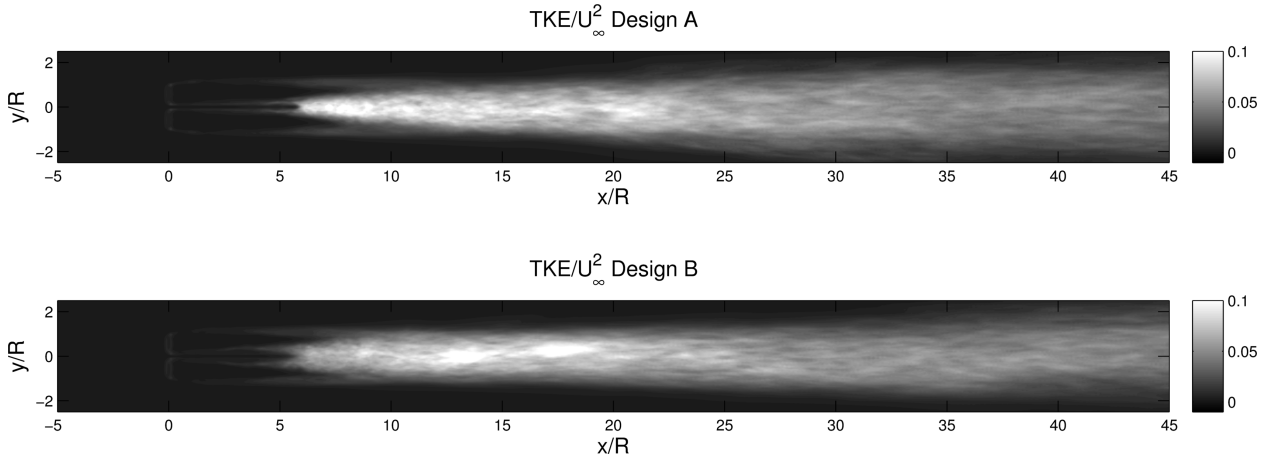


**Figure 14. Turbulent kinetic energy of fluctuating velocity components, $\frac{K}{U_\infty^2} = \frac{1}{2}\left(\overline{(\frac{U'}{U_\infty})^2} + \overline{(\frac{V'}{U_\infty})^2} + \overline{(\frac{W'}{U_\infty})^2}\right)$.**

### Effect of Time Step

To approximate the smallest turbulent length scale that can be resolved for the given number of time steps used per revolution, it can be shown that $\frac{\mathrm{d}l}{R} = \frac{2\pi}{(nti)\,\lambda}$. For these designs, this corresponds to a radius normalized length scale of $\frac{\mathrm{d}l}{R} = 0.14$ for $nti = 5$ and $\frac{\mathrm{d}l}{R} = 0.035$ for $nti = 20$. Figure 15 shows that the number of time steps used in the CACTUS simulation effects the recovery of momentum in the wake. However for time scales above $nti = 5$, the differences are much smaller. This means that the higher frequency time scales are not that important to the wake development. Five time steps per revolution is too few because the drag coefficient at the rotor plane is under predicted compared to the other cases. For 10 time steps per revolution, and more, the drag coefficients in the near wake ($0 < \frac{x}{R} < 5$) agree well, and the momentum recovery ($10 < \frac{x}{R} < 28$) agrees well between the cases. Ten time steps per revolution corresponds to a time step of 0.14 s.

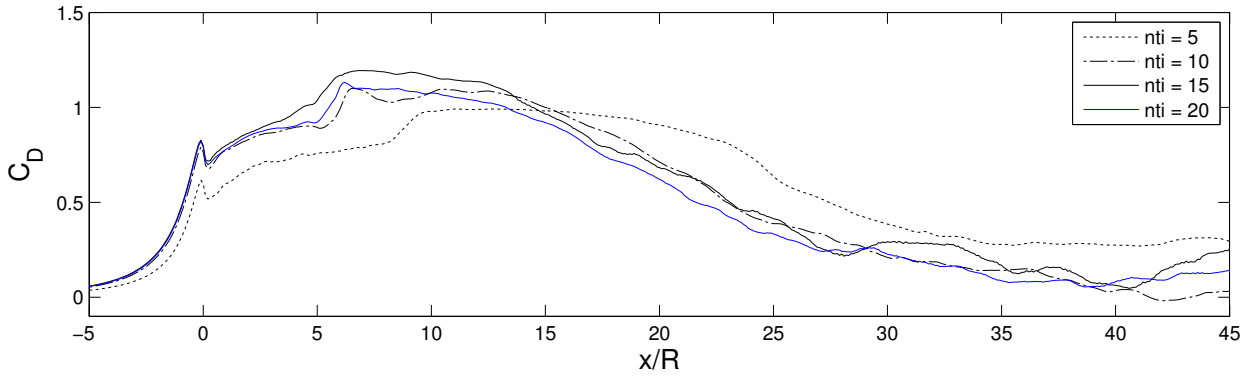


**Figure 15. The effect of number of time steps per revolution, $nti$, on momentum recovery.**

## IV. Conclusion

The recovery of freestream momentum in the far-wake region was significantly faster for design B. The momentum in the wake recovered to 90% of freestream by $\frac{x}{R} = 34.8$ for design A, and $\frac{x}{R} = 24.5$ for design B, a difference of over 10 rotor radii. The transition from near-wake to mid-wake, where the root vortex broke down was slightly sensitive to blade loading. But despite the root vortex breaking down first and more abruptly for design A, this did not help with momentum recovery. According to these free-wake vortex simulations, blade designs with larger spanwise gradients of bound circulation and larger induced angular velocity exhibit shorter and faster mixing far-wakes (but not necessarily the transition to mid-wake.) The design which produced a shorter wake, however, has a non-optimal efficiency. Future plans include an optimization study of the blade loading distribution to optimize energy capture for a wind farm by trading off individual rotor efficiency, $C_P$, for closer inter-turbine spacing by reducing the wake recovery distance. In addition, smaller time scales will be run in CACTUS to account for the discrepancy with LES and the region of maximum turbulent kinetic energy. And finally it will be shown if the enhanced wake recovery is eliminated, or to what extent reduced, by adding freestream turbulence and shear.

# References


[1]Jensen, N. O., "A Note on Wind Generator Interaction," Tech. Rep. M-2411, Risø DTU National Laboratory, 1983.

[2]Frandsen, S., Barthelmie, R., Pryor, S., Rathmann, O., Larsen, S., Højstrup, J., and Thøgersen, M., "Analytical modelling of wind speed deficit in large offshore wind farms," *Wind Energy*, Vol. 9, No. 1-2, 2006, pp. 39–53.

[3]Vermeer, L. J., Sørensen, J. N., and Crespo, A., "Wind Turbine Wake Aerodynamics," *Progress in Aerospace Sciences*, 2003, pp. 467–510.

[4]Sørensen, J. N. and Shen, W. Z., "Numerical Modeling Of Wind Turbine Wakes," *Journal of Fluids Engineering*, Vol. 124, 2002, pp. 393–399.

[5]Simoes, F. J. and Graham, J. M. R., "Prediciton Of Loading On A Horizontal Axis Wind Turbine Using A Free Vortex Wake Model," *BWEA Conference*, 1991.

[6]Miller, R. H., "The Aerodynamic and Dynamic Analysis of Horizontal Axis Wind Turbines," *Journal of Wind Engineering and Industrial Aerodynamics*, Vol. 15, 1983, pp. 329–340.

[7]Bareiss, R. and Wagner, S., "A Hybrid Wake Model for HAWT," *AIAA Proceedings for Navier-Stokes, full potential, and free wake method for rotor flows*, No. 0401, 1997.

[8]Afjeh, A. A. and Keith, T. G., "A Simplified Free Wake Method For Horizontal-Axis Wind Turbine Performance Prediction," *ASEM Journal of Fluids Engineering*, , No. 108, 1986, pp. 303–309.

[9]Maniaci, D., *Wind Turbine Design Using A Free-wake Vortex Method With Winglet Application*, Ph.D. thesis, Pennsylvania State University, 2012.

[10]Voutsinas, S. G., Beleiss, M. A., and Rados, K. G., "Investigation of the Yawed Operation of Wind Turbines by Means of a Vortex Particle Method," *AGARD Conference Proceedings*, No. 552, 1995.

[11]Strickland, J. H., Webster, B. T., and Nguyen, T., "A Vortex Model of the Darrieus Turbine: An Analytical and Experimental Study," *Journal of Fluids Engineering*, Vol. 101, No. 4, 1979, pp. 500.

[12]Strickland, J. H., Smith, T., and Sun, K., "A Vortex Model of the Darrieus Turbine: An Analytical and Experimental Study," Tech. Rep. SAND81-7017, Sandia National Laboratories, 1981.

[13]Murray, J. C. and Barone, M., "The Development of CACTUS, a Wind and Marine Turbine Performance Simulation Code," *AIAA 49th Aerospace Sciences Meeting*, No. 147, 2011.

[14]Leishmann, J. G. and Beddoes, T. S., "A Semi-Empirical Model for Dynamic Stall," *Journal of the American Helicopter Society*, Vol. 34, No. 3, 1989, pp. 3–17.

[15]Gormont, R. E., "A Mathematical Model of Unsteady Aerodynamics and Radial Flow for Application to Helicopter Rotors," Tech. Rep. 7322, US Army Air Mobility R&D, 1973.

[16]Michelen, C., Murray, J., and Neary, V., "Model Performance Evaluation of CACTUS," Tech. rep., Sandia National Labs, 2013.

[17]Burton, T., Jenkins, N., Shapre, D., and Bossyanyi, E., *Wind Energy Handbook*, Wiley, 2nd ed., 2011.

[18]Jamieson, P., *Innovation in Wind Turbine Design*, Wiley, 2011.

[19]Kang, S., Y. X. and Sotiropoulos, F., "On the onset of wake meandering for an axial flow turbine in a turbulent open channel flow," *Journal of Fluid Mechanics*, Vol. 744, No. 376–403, 2014.

[20]53rd AIAA Aerospace Sciences Meeting, *Effects of spanwise blade load distribution on wind turbine wake evolution*, 2015.